

Accuracy of Stellar Mass-to-light Ratios of Nearby Galaxies in the Near-Infrared

TAEHYUN KIM,¹ MINJIN KIM,¹ LUIS C. HO,^{2,3} YANG A. LI,⁴ WOONG-SEOB JEONG,^{5,6} DOHYEONG KIM,⁷
YONGJUNG KIM,⁵ BOMELEE,⁵ DONGSEOB LEE,⁸ JEONG HWAN LEE,^{1,9,10} JEONGHYUN PYO,⁵ HYUNJIN SHIM,⁸
SUYEON SON,¹ HYUNMI SONG,¹¹ AND YUJIN YANG^{5,6}

¹*Department of Astronomy and Atmospheric Sciences, Kyungpook National University, Daegu 41566, Republic of Korea*

²*Kavli Institute for Astronomy and Astrophysics, Peking University, Beijing 100871, People's Republic of China*

³*Department of Astronomy, School of Physics, Peking University, Beijing 100871, People's Republic of China*

⁴*Department of Astronomy, School of Physics and Astronomy, Shanghai Jiao Tong University, Shanghai 200240, People's Republic of China*

⁵*Korea Astronomy and Space Science Institute, Daejeon 34055, Republic of Korea*

⁶*University of Science and Technology, Korea, Daejeon 34113, Republic of Korea*

⁷*Department of Earth Sciences, Pusan National University, Busan 46241, Republic of Korea*

⁸*Department of Earth Science Education, Kyungpook National University, Daegu 41566, Republic of Korea*

⁹*Department of Physics and Astronomy, Seoul National University, 1 Gwanak-ro, Gwanak-gu, Seoul 08826, Republic of Korea*

¹⁰*Research Institute of Basic Sciences, Seoul National University, Seoul, 08826, Republic of Korea*

¹¹*Department of Astronomy and Space Science, Chungnam National University, Daejeon 34134, Republic of Korea*

ABSTRACT

Future satellite missions are expected to perform all-sky surveys, thus providing the entire sky near-infrared spectral data and consequently opening a new window to investigate the evolution of galaxies. Specifically, the infrared spectral data facilitate the precise estimation of stellar masses of numerous low-redshift galaxies. We utilize the synthetic spectral energy distribution (SED) of 2853 nearby galaxies drawn from the DustPedia (435) and Stripe 82 regions (2418). The stellar mass-to-light ratio (M_*/L) estimation accuracy over a wavelength range of 0.75–5.0 μm is computed through the SED fitting of the multi-wavelength photometric dataset, which has not yet been intensively explored in previous studies. We find that the scatter in M_*/L is significantly larger in the shorter and longer wavelength regimes due to the effect of the young stellar population and the dust contribution, respectively. While the scatter in M_*/L approaches its minimum (~ 0.10 dex) at $\sim 1.6 \mu\text{m}$, it remains sensitive to the adopted star formation history model. Furthermore, M_*/L demonstrates weak and strong correlations with the stellar mass and the specific star formation rate (SFR), respectively. Upon adequately correcting the dependence of M_*/L on the specific SFR, the scatter in the M_*/L further reduces to 0.02 dex at $\sim 1.6 \mu\text{m}$. This indicates that the stellar mass can be estimated with an accuracy of ~ 0.02 dex with a prior knowledge of SFR, which can be estimated using the infrared spectra obtained with future survey missions.

Keywords: Galaxies; Stellar masses; Infrared astronomy

1. INTRODUCTION

The stellar mass is one of the most fundamental parameters that offer crucial insights into the formation and evolution of galaxies. Furthermore, it helps probe the mass assembly history of galaxies through the stellar mass function (e.g., Madau & Dickinson 2014). In

addition, its correlations with other physical properties of galaxies (e.g., metallicity, size, halo mass, and the mass of the central supermassive black hole) help facilitate the detailed evolution of galaxies (e.g., Maiolino & Mannucci 2019; Wechsler & Tinker 2018; Kormendy & Ho 2013; Conselice 2014). Therefore, robust estimations of the stellar mass are crucial for understanding the detailed evolution of the galaxy.

The stellar mass for a large number of samples has conventionally relied on broad-band photometry, assum-

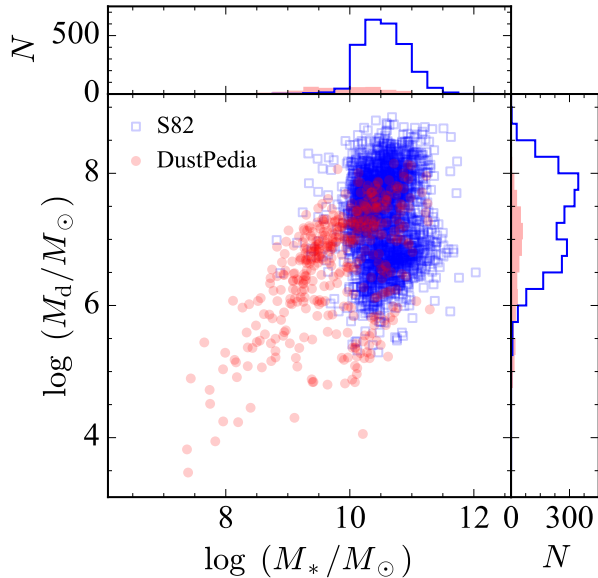


Figure 1. Distributions of stellar and dust masses derived from the SED fitting of multi-wavelength data spanning the UV to FIR. Red circles denote the sample from the DustPedia, and blue squares represent the sample from the SDSS S82 (Li et al. 2023).

ing a constant mass-to-light ratio (M_*/L) for a given broad-band filter. In line with these practices, M_*/L , known to depend on the stellar age, metallicity, initial mass function (IMF), and dust extinction, was theoretically or semi-empirically derived using the stellar population model (e.g., Larson & Tinsley 1978; Bell et al. 2003; Bruzual & Charlot 2003; Zibetti et al. 2009; Taylor et al. 2011). As those properties cannot be directly measured with ease, a color index has been widely used as a secondary parameter to infer M_*/L . While the accuracy of this method strongly depends on the effective wavelength of the filter, the scatter in M_*/L is $\sim 0.1 - 0.2$ dex (e.g., Bell et al. 2003; Zibetti et al. 2009; Taylor et al. 2011; Into & Portinari 2013; Roediger & Courteau 2015). Note that this scatter does not account for systematics arising from uncertainties in the stellar population models, which can be up to $0.1 - 0.4$ dex (e.g., Conroy 2013; Hon et al. 2022). This effect, specifically in NIR ($0.75 - 5 \mu\text{m}$), is examined in another study (Lee et al., submitted). Alternatively, M_*/L is often estimated using spectral energy distributions (SED) constructed from multiple broad-band photometric data (Conroy 2013). In this approach, synthetic SEDs are modeled with varying star formation history (SFH), which can introduce additional uncertainty in the stellar mass estimation. This uncertainty becomes more significant when photometric coverage is limited.

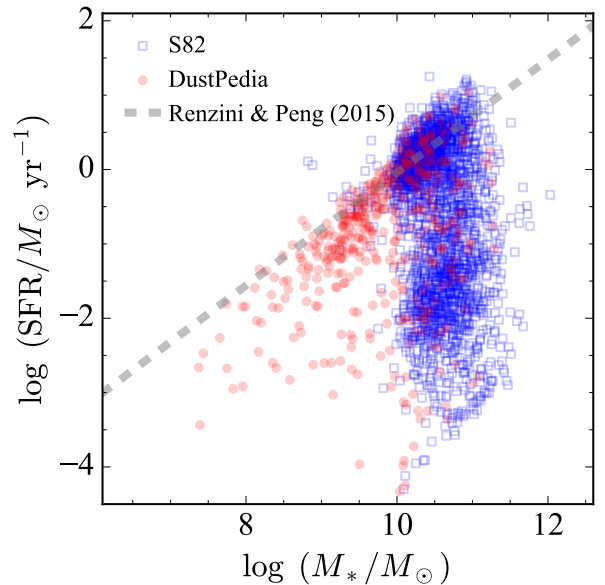


Figure 2. Distributions of stellar masses and SFRs derived from the SED fitting of multi-wavelength data spanning the UV to FIR. The symbols are the same as in Figure 1. The dashed line denotes the star-formation main sequence of nearby galaxies at $0.02 < z < 0.08$ (Renzini & Peng 2015).

Photometric data from the near-infrared (NIR) spectral regions are particularly useful to robustly estimate the stellar mass, as it is minimally affected by the dust attenuation and the M_*/L ratio is less sensitive to the stellar age compared to those from the UV/optical data (Into & Portinari 2013). However, intermediate-age stars such as those on the thermally pulsating asymptotic giant branch (TP-AGB) can significantly contribute to the fluxes in the NIR (e.g., Meidt et al. 2012), underscoring that the accuracy of the stellar mass estimation is closely tied to the reliability of the stellar population models in the NIR (e.g., Taylor et al. 2011; Conroy 2013). For example, K -band photometric data combined with M/L_K can be a powerful tool for the stellar mass estimation in the local Universe (e.g., Bell et al. 2003). In addition, NIR photometric data predominantly extracted from the *Spitzer* Space Telescope (Werner et al. 2004) and the WISE mission (Wright et al. 2010) contributed significantly to the stellar mass estimation of relatively nearby galaxies (e.g., Meidt et al. 2014; Querejeta et al. 2015; Jarrett et al. 2023). Notably, NIR-based M_*/L above $3\mu\text{m}$ are easily contaminated by the emission lines and continuum originating from the warm dust, which requires empirical corrections using the NIR colors (e.g., W1-W2 or IRAC1-IRAC2). However, the complex contributions from the $3.3 \mu\text{m}$ polycyclic aromatic hydrocarbon (PAH) emission to the W1 and IRAC1 bands complicate the dust-contamination

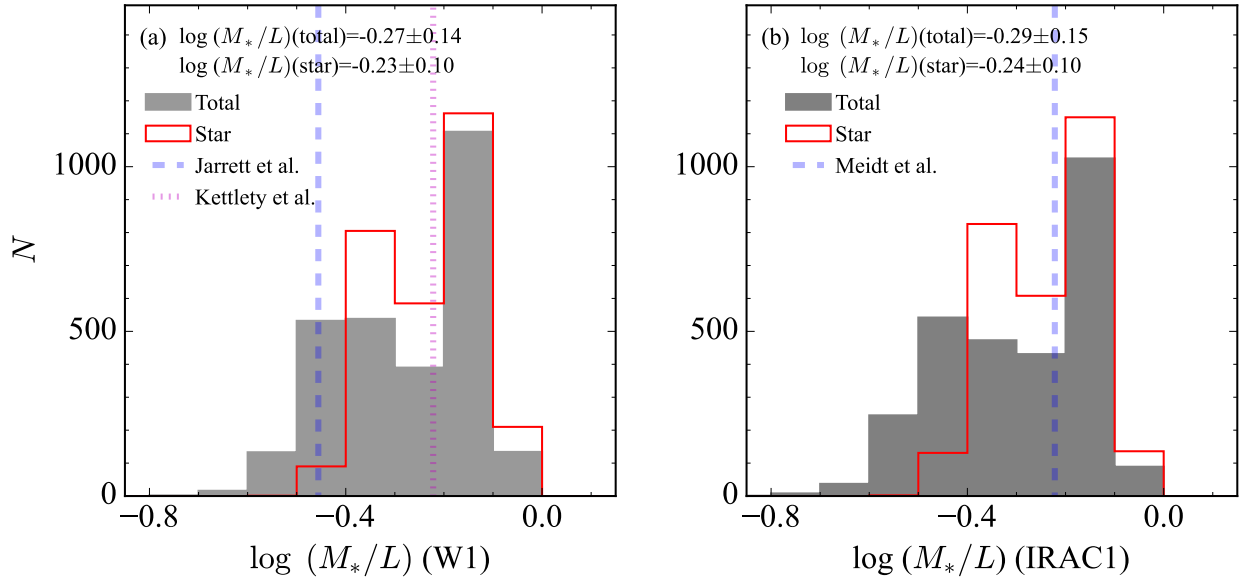


Figure 3. Distributions of M_*/L ratios at the W1 (a) and IRAC1 (b) bands. The gray-shaded histograms represent M_*/L derived from the total luminosity, encompassing stellar light, dust emissions, and nebular emissions. The red open histograms denote M_*/L derived using the stellar luminosity. Mean and standard deviation values are shown in each panel. (a) The red dotted and blue dashed lines indicate M_*/L from Kettlety et al. (2018) and Jarrett et al. (2023), respectively. (b) The blue dashed line denotes M_*/L from Meidt et al. (2014).

corrections solely based on NIR colors (e.g., Lee et al. 2012; Yamada et al. 2013; Inami et al. 2018; Lai et al. 2020), potentially introducing systematic uncertainties on the stellar mass estimations. Collectively, these effects can limit the accuracy of the stellar mass estimations based on NIR broad-band photometric data.

Upcoming satellite missions, including The Spectro-Photometer for the History of the Universe, Epoch of Reionization and Ices Explorer (SPHEREx), are poised to enrich our understanding of the Universe (Korngut et al. 2018; Crill et al. 2020). In particular, SPHEREx will conduct an all-sky survey with linear variable filters, providing the all-sky spectral data spanning a wavelength range of $0.75 - 5 \mu\text{m}$ with spectral resolutions of $\sim 40 - 130$ (Doré et al. 2016; Crill et al. 2020). This extensive dataset will enable us to estimate the stellar mass of numerous galaxies, which is crucial to understanding the galaxy evolution in the nearby Universe. Furthermore, leveraging its wide wavelength coverage and spectral capabilities, this NIR dataset is expected to facilitate precise stellar-mass estimations. However, the NIR spectral range ($1-5 \mu\text{m}$) remains relatively underexplored owing to limited observational data (Brown et al. 2014).

Based on the above backgrounds, we investigate the M_*/L within the spectral range of $0.75 - 5.0 \mu\text{m}$, covered by SPHEREx, which will provide the low spectral resolution ($R \sim 40$) data. For that purpose, we utilize the synthetic SED obtained from the SED fitting of the

multi-wavelength data of nearby galaxies adopted from literature. The sample selection and adopted dataset are summarized in Section 2. The NIR-based M_*/L estimations are calculated in Section 3. The estimation accuracy of the obtained M_*/L ratio is described in Section 4. In Section 5, we summarize the conclusions of this study. Throughout the paper, we adopt the cosmological parameters: $H_0 = 100h = 70 \text{ km s}^{-1} \text{ Mpc}^{-1}$ and $\Omega_\Lambda = 0.7$. All magnitudes are given in the Vega system.

2. SAMPLE AND DATA

2.1. Sample Selection

To utilize the SED derived from the observed photometric dataset, we first employ the sample from the DustPedia (Davies et al. 2017; Clark et al. 2018). The multi-wavelength dataset of the DustPedia spanning the UV to far-infrared (FIR) enables robust estimations of both stellar population and dust properties through SED fitting with the Code Investigating GALaxy Emission (CIGALE) code (Boquien et al. 2019). This characteristic makes the DustPedia sample ideal for our study (Nersesian et al. 2019). The DustPedia constructed the SEDs based on the aperture-matched photometry on the 42 bands data covering UV to sub-mm, obtained from the Herschel observation, along with the archival observations from the GALEX, SDSS, 2MASS, WISE, *Spitzer*, and *Planck*. The original DustPedia sample contains 875 nearby galaxies with $D_L \leq 79 \text{ Mpc}$. However, this Dust-

Pedia sample is slightly biased toward low-mass galaxies ($\langle M_* \rangle = 10^{9.7 \pm 0.95} M_\odot$) because of their proximity.

To compensate for this limitation, we additionally adopt a sample of nearby ($0.01 \leq z \leq 0.11$) massive galaxies from Li et al. (2023), which employed data from the SDSS Stripe 82 region (S82). Li et al. (2023) conducted the sophisticated photometry on the multi-wavelength imaging data of 2685 massive galaxies ($10^{10} M_\odot \lesssim M_* \lesssim 10^{11.5} M_\odot$). As the initial sample selection was based on stellar mass estimates from the GALEX–SDSS–WISE Legacy Catalog (GSWLC-2; Salim et al. 2018), a small fraction of the S82 sample finally shows $M_* < 10^{10} M_\odot$. These data encompassed UV, optical, NIR, MIR, and FIR data obtained from GALEX, SDSS, 2MASS, WISE, and Herschel-SPIRE, respectively. The matched-aperture and profile-fitting photometry were applied for the shorter-wavelength bands ranging from UV to W2 and the longer-wavelength bands, respectively. In addition, multi-band imaging decomposition was carefully performed to accurately remove the contribution from neighboring galaxies or foreground stars. These procedures resulted in reliable flux measurements and precise estimations of the uncertainties of the multi-wavelength dataset. From the comparison with the photometric data of GALEX, SDSS, and 2MASS extended source catalogs (Jarrett et al. 2000), Li et al. (2023) showed that their measurements agree within ± 0.1 mag in the UV, optical, and NIR bands. However, the photometric measurements of Li et al. (2023) are systematically brighter ($\sim 0.2 - 1.0$ mag) than those in 2MASS point source catalog (Cutri et al. 2003) and ALLWISE, in which the photometric data were originally estimated from a PSF-fitting method. Notably, these systematic discrepancies are significantly reduced up to ≤ 0.2 mag when compared with the unWISE catalog (Lang et al. 2016).

2.2. SED Fitting

For the S82 sample, stellar and dust masses are drawn from Li et al. (2023). These parameters were obtained via SED fitting using the CIGALE. In this SED fitting process, the stellar SED was modeled using the simple stellar population (SSP) from Bruzual & Charlot (2003). The stellar population was modeled with a double-exponential SFH, comprising an old stellar population with an age of 12 Gyr and a young stellar population with an age range from 10 to 5000 Myr. The stellar emission was modeled with metallicities of $0.004 - 0.02$. The IMF of Chabrier (2003) was adopted. In addition, the starburst attenuation curve from Calzetti et al. (2000) with a modification of the power-law slope was

adopted to account for the dust attenuation in the SED fitting.

Dust emission is modeled with $U_{\min} = 0.1 - 25$, $q_{\text{PAH}} = 2.5$ (fixed), $\gamma = 0.001 - 0.2$. Here, U_{\min} denotes the minimum radiation field from the stars; q_{PAH} represents the mass fraction of PAHs; γ indicates the mass fraction of dust illuminated from the minimum to maximum radiation field. α , the power-law slope of the dust continuum over the IR wavelength, is fixed to 2. Nebular emission lines were also included (Inoue 2011). The AGN component modeled with Fritz et al. (2006) was incorporated. Here, the AGN fraction (f_{AGN}) was calculated as the ratio of the AGN luminosity to the total IR luminosity estimated within $1 - 1000 \mu\text{m}$.

Whereas the SED fitting with the CIGALE was also applied to the DustPedia sample (Jones et al. 2013; Nersesian et al. 2019), parameters for the stellar population and dust modeling significantly differ from those of Li et al. (2023). In addition, contrary to the S82 sample, the SED fitting of the DustPedia sample did not consider any AGN components. To avoid possible systematics due to these factors, we perform the SED fitting on the DustPedia dataset. To maintain consistency, we adopt the same fitting parameters and bandpasses used for the S82 dataset. We exclude the photometric data contaminated by artifacts or nearby sources, as well as data obtained from the imaging data that partially covers the target source (Clark et al. 2018). To secure accurate stellar mass measurements from the SED fitting, samples lacking flux measurements in the optical band (*gri*) are further discarded. The systematic effects due to the discrepancy in the fitting parameters between the original DustPedia study (Nersesian et al. 2019) and this study are further discussed in Appendix A.

We discard the targets with a reduced χ^2 value exceeding 2 to ensure reliable assessments of the stellar and dust properties. Furthermore, following the recipe from Li et al. (2023), the AGNs defined as $f_{\text{AGN}} > 0.1$ were excluded, as the flux contribution from the AGN can introduce additional uncertainties. This results in the final samples containing 435 and 2418 galaxies from the DustPedia and S82, respectively. Throughout this study, we utilize the synthetic SEDs obtained from the best fit for magnitude estimations across various filters and wavelengths. The goodness-of-fit, particularly in NIR regions, is examined in Appendix B. The stellar masses derived from the SED fitting agree with those of GALEX–SDSS–WISE Legacy Catalog 2 (GSWLC-2; Salim et al. 2018) with $\Delta M_* = 0.01 \pm 0.11$ dex (Li et al. 2023). However, a moderate difference is observed in the star formation rate when compared to GSWLC-2 ($\Delta \log \text{SFR} = -0.12 \pm 0.56$ dex). As described in Li et

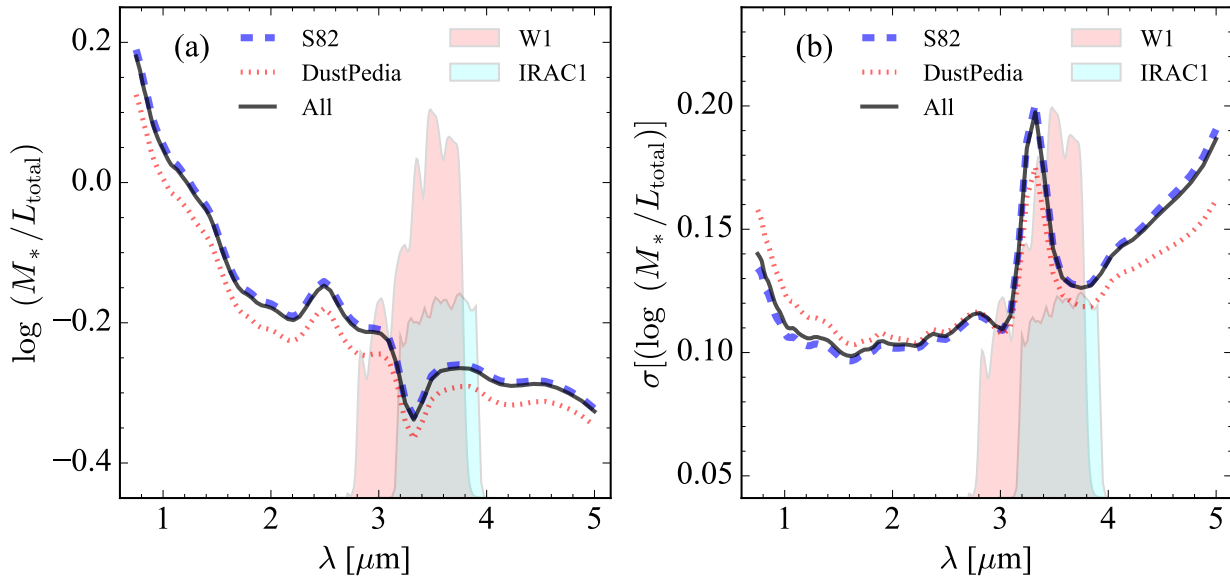


Figure 4. M_*/L ratios calculated using the total luminosity (a) and their scatters (b) as functions of the wavelength. Subsamples from DustPedia and S82 are denoted by a red dotted line and a blue solid line, respectively. The thick solid line represents M_*/L for the entire sample. The red and cyan areas denote transmission curves of W1 and IRAC1, respectively. Note that the unit of the transmission curves is arbitrary. Due to the 3.3 μm PAH emission, there appears to be a dip and a bump at 3.3 μm of the M_*/L value and the scatter, respectively.

al. (2023), this discrepancy arises from the differences in the methods of photometric measurements, particularly in the mid- and far-infrared bands.

Figure 1 illustrates the distributions of stellar and dust masses determined from the SED fitting process, demonstrating the complementary characteristics of the two subsamples in the two-parameter space. Furthermore, our sample covers a wide range of SFR at a given stellar mass, from the star-forming main sequence to relatively quiescent galaxies, which is crucial to investigate the variations in the M_*/L ratio with various properties of galaxies (Fig. 2).

3. RESULTS

3.1. Mass-to-Light Ratio in Broadband Photometry

Conventionally, stellar-mass estimations in the NIR band (3 – 5 μm) have been based on broadband photometry obtained from the *Spitzer* Space Telescope and the WISE mission. As the first step of our analysis, we compute M_*/L at commonly used broadband filters in the NIR (e.g., IRAC1 and W1). Figure 3 shows M_*/L at IRAC1 and W1 using the stellar and total luminosities. Overall, we can estimate the stellar mass with an accuracy of 0.14 – 0.15 dex solely with the NIR data, which is consistent with the previous studies (e.g. Meidt et al.

2014; Kettley et al. 2018; Jarrett et al. 2023).¹ However, as the dust continuum and 3.3 μm PAH emission can contribute to the total luminosity in those filters, the M_*/L ratios calculated using the total luminosity exhibit a substantially larger scatter compared to those calculated using the stellar luminosity.

Meanwhile, considering only the stellar light, the scatter in M_*/L can be significantly reduced down to ~ 0.10 dex. While the average M_*/L ratio at IRAC 1 [$M_*/L \sim 0.58$ or $\log(M_*/L) \sim -0.24$] is in good agreement with the prediction for the old stellar population ($M_*/L \sim 0.60$; Meidt et al. 2014; Querejeta et al. 2015), that at the W1 band [$M_*/L \sim 0.54$ ($\log(M_*/L) \sim -0.27$) and ~ 0.59 ($\log(M_*/L) \sim -0.23$) from the total and stellar luminosity, respectively] is significantly larger than the empirically derived value for the nearby galaxies ($M_*/L \sim 0.35$; Jarrett et al. 2023). Note that M_*/L in Jarrett et al. (2023) is derived from the W1 total luminosity. With the EAGLE simulations, Norris et al. (2016) examined the M/L distribution of simulated early-type/quiescent galaxies and found $M_*/L \sim 0.85$, which is in good agreement with a peak in the higher M_*/L found in the distribution of M_*/L (Fig. 3). While

¹ It is worthwhile to note that this accuracy is calculated relative to the stellar mass derived from the SED fitting performed using the parameterized SFH, potentially introducing a zero-point offset of up to 0.3 – 0.4 dex. This bias, however, is not considered in this study (e.g. Conroy 2013; Lower et al. 2020).

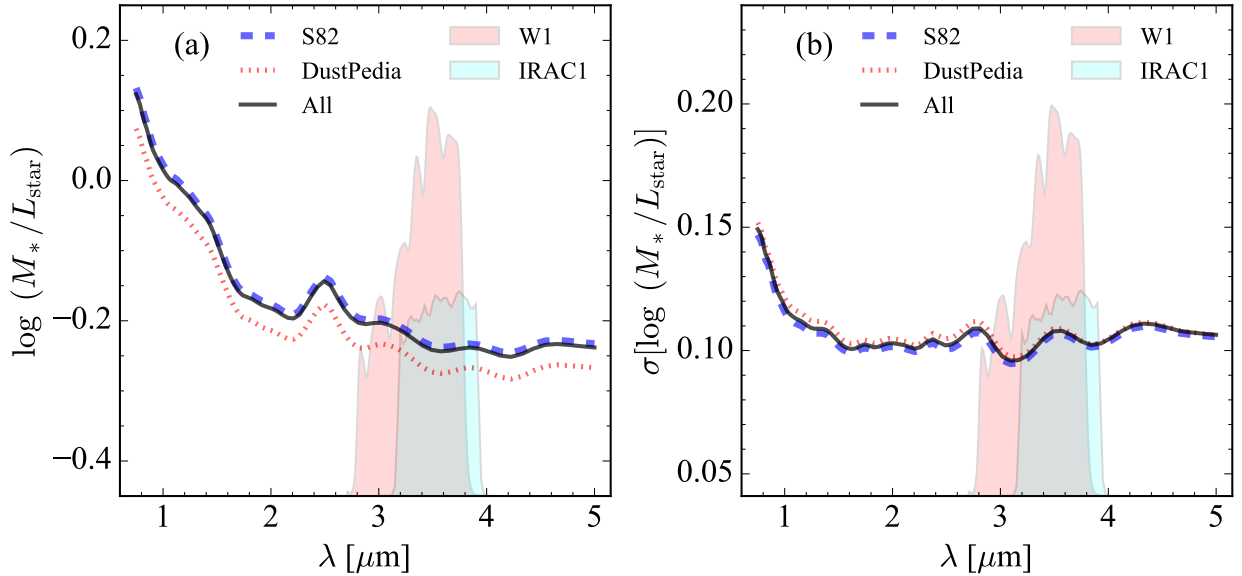


Figure 5. M_*/L calculated using the stellar luminosity (a) and their scatters (b) as functions of the wavelength. The symbols are the same as in Figure 4.

the origin of this discrepancy remains rather unclear, it can be partially attributed to differences in flux measurements across the chosen datasets. Specifically, the dedicated flux measurements of the WISE dataset obtained from Li et al. (2023) are systematically brighter by 0.2 – 0.5 mag compared to the ALLWISE measurements based on profile-fitting results, which was used to estimate the M_*/L values in Jarrett et al. (2023). Interestingly, in our study, the M_*/L values calculated for W1 and IRAC1 are consistent with each other, which supports the reliability of our estimates. It is also worthwhile noting that, unlike other studies, Jarrett et al. (2023) used the observed total luminosity, instead of the stellar luminosity, to calculate the M_*/L values, naturally resulting in a low M_*/L .

3.2. Mass-to-Light Ratio in Spectral Data

As the NIR spectral data will be obtained through future space missions, such as SPHEREx, investigating the M_*/L in these spectral elements is worthwhile. To this end, we employ 68 spectral components with a spectral resolution of 40 (i.e., $\lambda/\Delta\lambda \approx 40$, where $\Delta\lambda$ is the bandwidth of each spectral component), covering a wavelength range of 0.75–5.0 μm . For simplicity, the transmission curve of each spectral component is modeled using a Gaussian profile. Although this assumption does not exactly match the spectral channels of the SPHEREx, it is adequate for examining the overall trend of the M_*/L ratio as a function of the wavelength.

As expected, the M_*/L ratio is inversely proportional to the wavelength because the M_*/L ratios in the shorter wavelengths are more sensitive to the young stellar pop-

ulation compared to those at the longer wavelength. However, the scatter of the M_*/L ratio exhibits a U-shaped pattern. The M_*/L values calculated using the total luminosity are significantly affected at longer wavelengths due to the existence of the dust continuum and PAH emission (Fig. 4). In particular, the excess in the scatter is remarkable around 3.3 μm , highlighting the need for the careful removal of the PAH emission to facilitate accurate stellar mass estimations. This effect can be rigorously quantified using the spectral dataset provided by the SPHEREx mission, particularly for star-forming galaxies (e.g. Xie et al. 2018a,b; Zhang et al. 2021).

In addition, the M_*/L values in the DustPedia sample are systematically smaller than those in the S82 sample. The M_*/L values are known to be strongly dependent on the specific SFR (e.g., Portinari et al. 2004). The DustPedia sample tends to have a larger specific SFR than the S82 sample (see §4.2), which may be the main cause of smaller M_*/L values for the DustPedia sample.

The scatter in the M_*/L ratios calculated from the stellar luminosity is significantly reduced (Fig. 5). At wavelengths longer than 1 μm , the overall scatter ranges between 0.1 and 0.11 dex, demonstrating a weak dependence on the wavelength. This indicates that the NIR spectrum is valuable for constraining the stellar mass almost regardless of the wavelength if the dust component can be adequately removed. The M_*/L values and their scatter for both subsamples are summarized in Table 1.

4. DISCUSSION

4.1. Dust Contribution to NIR Photometry

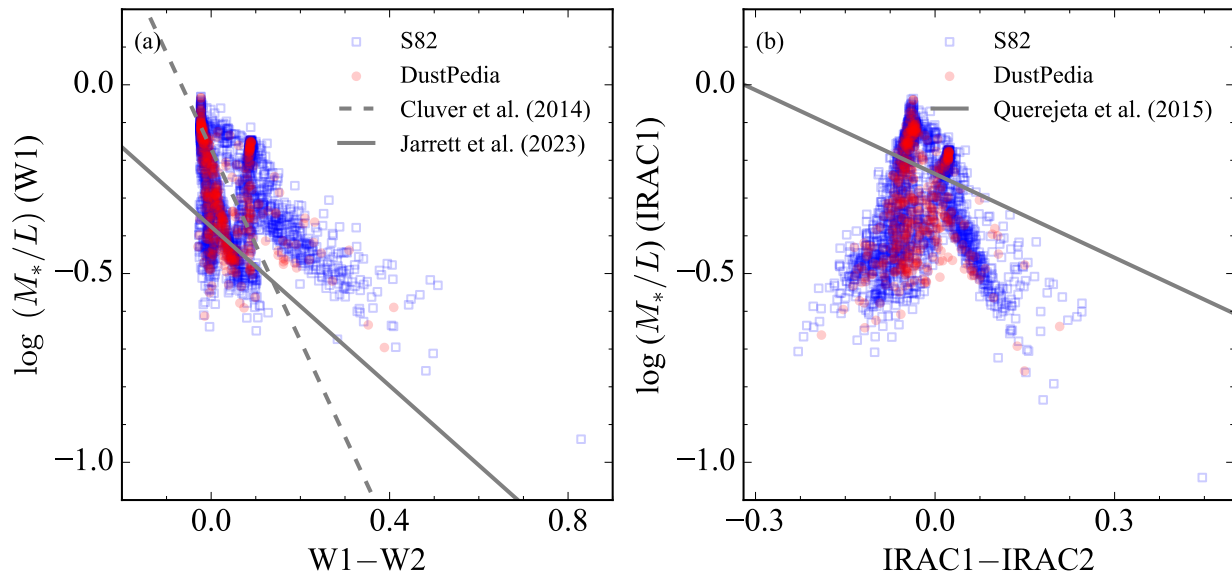


Figure 6. Dependence of M_*/L calculated using the total luminosity on the W1–W2 color (a) and IRAC1–IRAC2 color (b). (a) The dashed line represents the empirical relation between M_*/L and the W1–W2 color for $z \sim 0.5$ galaxies from GALAXY AND MASS ASSEMBLY (GAMA) survey (Cluver et al. 2014). The solid line denotes the newly calibrated relation for nearby galaxies at $z \sim 0.15$ from the GAMA survey (Jarrett et al. 2023). (b) The solid line represents the relation based on the sample from the Spitzer Survey of Stellar Structure in Galaxies (S⁴G; Querejeta et al. 2015).

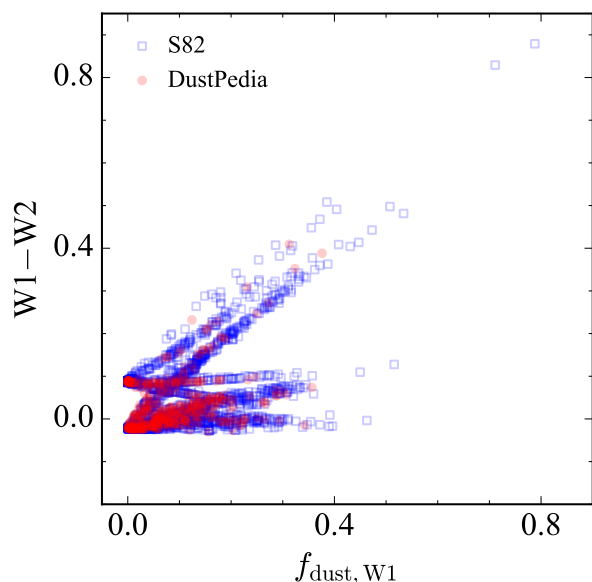


Figure 7. W1–W2 color as a function of the ratio of the dust flux to the total flux at the W1 band. The symbols are the same as in Figure 1.

The NIR colors (IRAC1–IRAC2 or W1–W2) have been utilized to approximate the light contribution from the dust, which needs to be adequately subtracted to estimate the stellar mass precisely. The basic assumption of this procedure is that the dust continuum is intrinsically redder than the stellar continuum. According to this assumption, Querejeta et al. (2015) and Jarrett

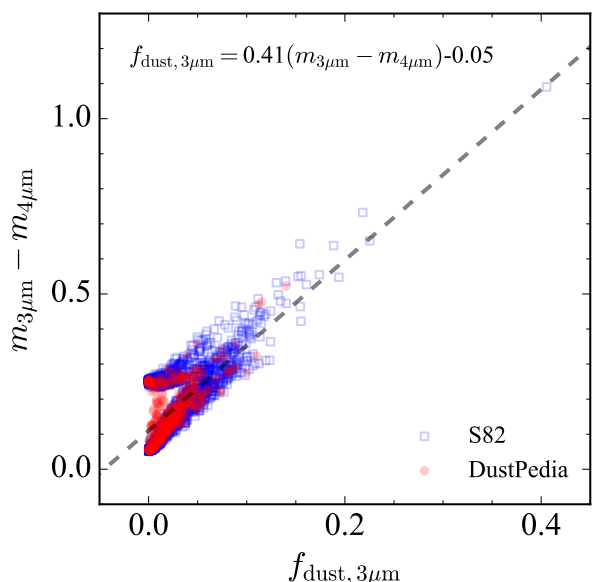


Figure 8. Correlation between the flux ratio the dust at $3 \mu\text{m}$ ($f_{\text{dust},3\mu\text{m}}$) and the color index between $3 \mu\text{m}$ and $4 \mu\text{m}$ ($m_{3\mu\text{m}} - m_{4\mu\text{m}}$). The dashed line denotes the linear fit to the data.

et al. (2023) demonstrated that M_*/L is inversely proportional to both the IRAC1–IRAC2 and W1–W2 colors, respectively. Here, we examine the validity of this finding for our dataset. We find two sequences in the plane of M_*/L and W1–W2 color for our sample (Fig. 6). In one sequence, consistent with the findings of previous studies, M_*/L is mildly anti-correlated with the

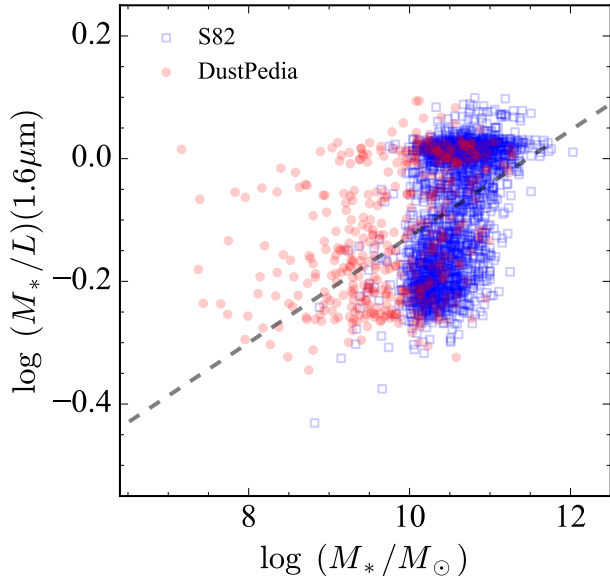


Figure 9. Correlation between M_*/L and stellar mass (M_*) at $\sim 1.6 \mu\text{m}$. Note that M_*/L is calculated using the stellar luminosity. The dashed line represents the linear regression fit to the entire data.

W1-W2 and IRAC1-IRAC2 color. Although this correlation broadly agrees with the general trend in earlier studies (e.g., Cluver et al. 2014; Jarrett et al. 2023), the observed relation between the two quantities deviates from those of previous studies. We attribute this to the fact that the photometric measurements of W1 and W2 adopted in this study are systematically brighter than the ALLWISE measurements (Li et al. 2023).

However, in another sequence, M_*/L is almost independent of the W1-W2 color, with a substantially large scatter. To comprehend this finding, we compare the NIR color with the ratio of the flux from the dust components to the total flux (f_{dust}) at the W1 band. Figure 7 shows that the dust fraction at the W1 band is only weakly correlated with the W1-W2 color. The hot and warm dust ($T \sim 300 - 500 \text{ K}$) from the star-forming regions can naturally increase the W1-W2 color (e.g., Xie et al. 2018a). Conversely, the prominent $3.3 \mu\text{m}$ PAH emission can boost the flux only at the W1 band, making the W1-W2 color bluer. Because the strength of the $3.3 \mu\text{m}$ PAH emission is proportional to the SFR but with a significant amount of the scatter, the correlation between the W1-W2 color and the dust fraction can be excessively intricate due to the competition between the dust continuum and PAH emission. This complexity cannot be quantified without a spectroscopic dataset (e.g., Yamada et al. 2013; Shim et al. 2023). A similar trend (i.e., a non-linear correlation between the

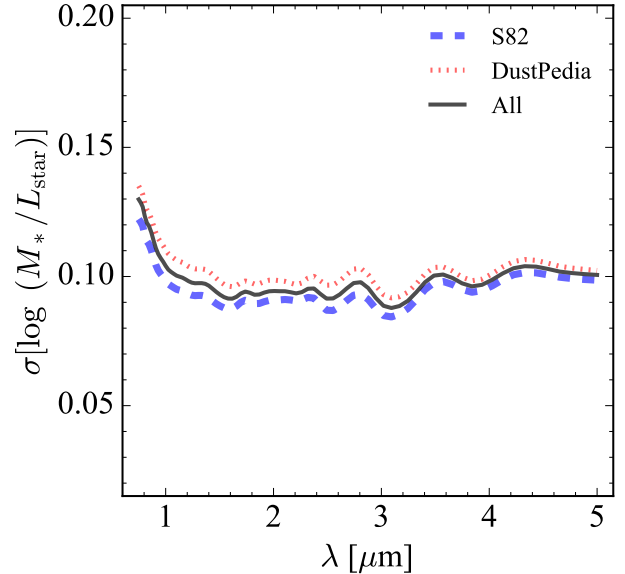


Figure 10. Scatter in M_*/L after correcting the correlation between M_*/L and the stellar mass (M_*). The symbols are the same as in Figure 4.

dust fraction and the NIR color) is also shown in the IRAC1-IRAC2 color.

As SPHEREx will provide the spectral information, the spectral color can serve as a better tracer for the dust contribution. Here, we adopt a color index between $3 \mu\text{m}$ and $4 \mu\text{m}$ ($m_{3\mu\text{m}} - m_{4\mu\text{m}}$) to avoid the strong $3.3 \mu\text{m}$ emission and compare it with the flux ratio of the dust at $3 \mu\text{m}$ ($f_{\text{dust},3\mu\text{m}}$). We find that $f_{\text{dust},3\mu\text{m}}$ is strongly correlated with $m_{3\mu\text{m}} - m_{4\mu\text{m}}$ expressed as $f_{\text{dust},3\mu\text{m}} = -0.05 + 0.41(m_{3\mu\text{m}} - m_{4\mu\text{m}})$ (Fig. 8), indicating that the dust contribution can be approximately estimated with the spectral color index in SPHEREx dataset.

4.2. Main Driver of the Scatter in M_*/L

Given that the M_*/L ratios can be highly affected by the stellar properties of the galaxies, adopting a second parameter is often essential for robustly estimating the stellar mass. Previous studies have extensively adopted the color term as the second parameter (e.g., Bell et al. 2003; Into & Portinari 2013). To identify an alternative in the spectral analysis, we investigate the parameter predominantly deriving the scatter in M_*/L . Initially, we find that M_*/L is weakly correlated with the stellar mass itself, likely attributed to the dependence of the SFH on stellar mass. To account for this dependence, we perform a linear regression between the stellar mass and M_*/L at each wavelength as follows: $\log(M_*/L) = a + b \log(M_*/M_\odot)$ (see Figure 9 for an example). The fitting results as a function of the wavelength are summarized in Table 2. With this treatment, the scatter is mildly reduced by $\sim 0.01 - 0.02$ dex. Thus,

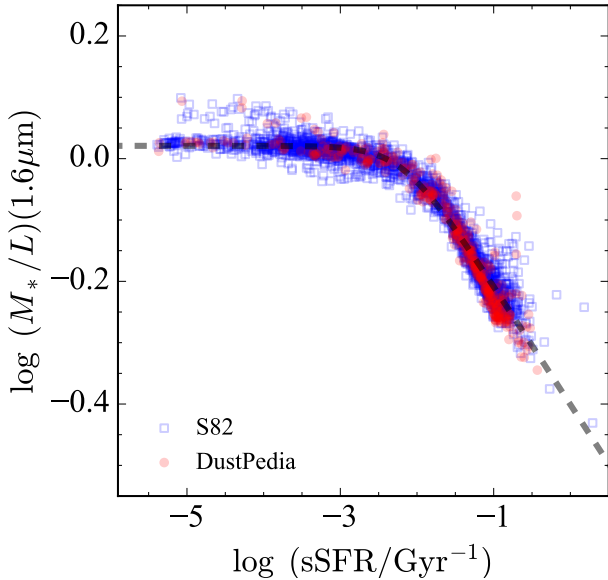


Figure 11. Correlation between M_*/L and the sSFR (i.e., SFR/M_*) at $\sim 1.6 \mu\text{m}$. Note that M_*/L is calculated using the stellar luminosity. The symbols are the same as in Figure 1. The relation can be well fitted with the smoothly broken power-law model (dashed line).

overall, with the NIR spectrum, the stellar mass can be estimated with a typical uncertainty of $\sim 0.09 - 0.1$ dex (Fig. 10).

Furthermore, the M_*/L ratio is tightly correlated with the SFR divided by the stellar mass, namely the specific star formation rate (sSFR). Figure 11 shows that this relation at $\sim 1.6 \mu\text{m}$ is well fitted with a smoothly broken power law, which is defined as:

$$\log(M_*/L) = a \left\{ \frac{1}{2} \left[1 + \left(\frac{\log \text{sSFR}}{\delta} \right)^{1/\beta} \right] \right\}^{-\alpha\beta}, \quad (1)$$

where a is the normalization factor [i.e., $\log(M_*/L)$ at $\text{sSFR} \ll \delta$], δ is the pivot sSFR, α is the power-law index at $\text{sSFR} > \delta$, and β is the smoothness parameter, which determines the smoothness of the power-law slope change around the pivot sSFR. Note that the unit of sSFR is Gyr^{-1} . Fitting results for various wavelengths are summarized in Table 3. This trend is rather expected from the adopted SFH with two components (old and young stellar populations) because the sSFR approximately traces the mass ratio of the old stellar population to the young stellar population. Considering this dependency, the scatter in M_*/L dramatically decreases to ~ 0.02 dex (Fig. 12). This result clearly demonstrates that more precise stellar mass estimations can be achieved using the known SFR. Note that the SFR used in this analysis is an instantaneous SFR provided by the CIGALE based on the star formation his-

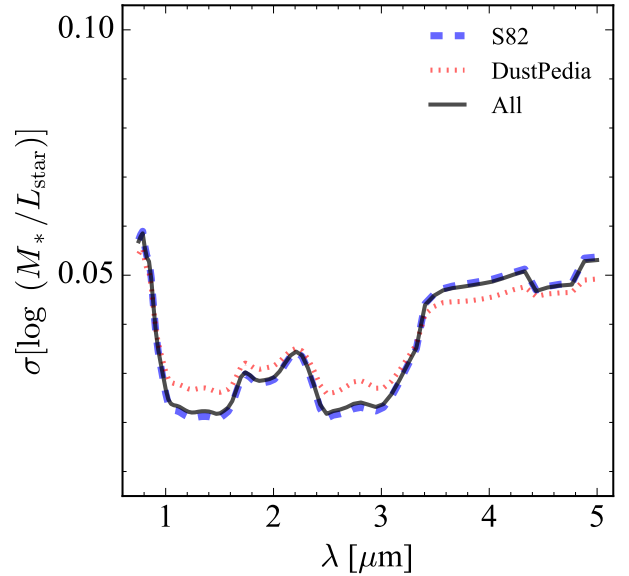


Figure 12. Scatter in M_*/L after correcting the correlation between M_*/L and the sSFR. The symbols are the same as in Figure 4.

tory. As the commonly used SFR indicators (e.g., hydrogen recombination lines) trace the average SFR over the last ~ 10 Myr, the observed SFRs may differ from those provided by CIGALE to some degree, which can introduce additional uncertainty in the M_*/L estimation (e.g., Byun et al. 2021).

4.3. Best Stellar Mass Indicator in NIR

Based on our calculations of M_*/L under various conditions, we attempt to identify an optimal method to estimate the stellar mass based on the NIR spectral data of nearby galaxies. If the contribution of the dust emission can be adequately removed from the observed spectrum, the scatter in the M_*/L ratio becomes almost independent of the wavelength. However, it is challenging to fit the PAH emissions and the dust continuum robustly, even using the NIR/MIR spectroscopic data (e.g. Xie et al. 2018a; Zhang & Ho 2023). Therefore, if available, NIR data around a wavelength of $1.6 \mu\text{m}$ are preferable, as will also be presented in Lee, J. H. et al. (submitted). This is because it is relatively free from dust contamination unless the AGN component is prominent, and the resulting scatter in M_*/L is smaller or comparable to that achieved using NIR data.

As outlined in the previous section (§4.2), the scatter in M_*/L can be slightly reduced if the dependence of M_*/L on stellar mass is considered. To this end, the stellar mass can be estimated from M_*/L using the monochromatic luminosity and subsequently subjected to iterative fine-tuning. Specifically, the initial stellar mass is estimated from a constant M_*/L , following

which the correlation between the M_*/L ratio and stellar mass can be corrected using the initial stellar mass measurement to achieve a more precise stellar-mass estimation. However, this iterative process can reduce the uncertainty by only 0.01 – 0.02 dex. Conversely, if the SFR can be estimated based on the NIR spectral data, for example, from the fluxes of hydrogen recombination lines (e.g., Kennicutt & Evans 2012) or 3.3 μm PAH emissions (e.g. Kim et al. 2012; Lai et al. 2020; Belfiore et al. 2023), the scatter in the stellar mass estimation can be dramatically reduced based on the strong correlation between M_*/L and sSFR. It is worthwhile to note that 3.3 μm PAH-based SFR can be more uncertain compared to other SFR indicators (e.g., hydrogen lines, UV, and IR) as its brightness relative to IR luminosity is correlated with physical parameters of host galaxies, such as metallicity (e.g. Shim et al. 2023; Whitcomb et al. 2024). However, this correction must again follow an iterative procedure, as a prior stellar mass estimate is essential to compute the sSFR. An alternative argument is that SFR, rather than sSFR, could be used to trace M_*/L . However, we find that the scatter in the correlation between SFR and M_*/L is significantly larger than that for sSFR. Therefore, sSFR provides a more reliable estimate of M_*/L . In conclusion, the NIR spectrophotometry provided by the SPHEREx can improve the accuracy of stellar mass estimations.

5. CONCLUSION

To investigate the accuracy of the M_*/L ratio at the NIR continuum, we employ the synthetic SEDs of stellar populations and dust derived from the observed multi-wavelength data ranging from UV to FIR of nearby galaxies at $z < 0.11$. The SED fitting results for two subsamples from the DustPedia and the S82 regions are adopted for this purpose. The stellar masses of the sample are also calculated based on the SED fitting results. The followings are some key findings and conclusions of our study:

- The M_*/L ratios in the widely used NIR broadband filters (e.g., W1 and IRAC1) are heavily affected by the strength of the dust continuum and PAH emissions. Our results demonstrate that the variations in the M_*/L ratio resulting from this effect cannot be easily quantified using the NIR color (e.g., W1–W2 or IRAC1–IRAC2) because the relative contribution between the dust continuum and PAH emission is complicated. This sys-

tematics effect can be significantly alleviated using the color index of NIR spectral data.

- While M_*/L in the NIR spectral range is strongly correlated with the wavelength, the scatter in M_*/L as a function of the wavelength exhibits a U-shaped profile due to the dependence on the stellar age and dust features in the short and long wavelength, respectively.
- If the contribution from the dust component can be adequately excluded from the NIR spectrum, the scatter in M_*/L can be significantly reduced in the long wavelength region and remain nearly constant along the wavelength with a variation of 0.01 – 0.02 dex.
- M_*/L demonstrates a weak correlation with the stellar mass and a strong correlation with the sSFR. If this dependency is corrected appropriately, the scatter in M_*/L can be dramatically decreased up to 0.02 – 0.06 dex. Based on these findings, we conclude that the stellar mass can be most accurately estimated using spectral data around $\sim 1.6\mu\text{m}$, combined with SFR measurements.

1 We are grateful to the anonymous referee for construc-
 2 tive comments and suggestions that greatly improved
 3 our manuscript. This work was supported by the Na-
 4 tional Key R&D Program of China (2022YFF0503401),
 5 the National Science Foundation of China (11991052,
 6 12233001), the China Manned Space Project (CMS-
 7 CSST-2021-A04, CMS-CSST-2021-A06), and the Na-
 8 tional Research Foundation of Korea (NRF), through
 9 grants funded by the Korean government (MSIT)
 10 (Nos. 2022R1A4A3031306, 2023R1A2C1006261, RS-
 11 2023-00240212, and RS-2024-00347548). Y. K. was sup-
 12 ported by the National Research Foundation of Ko-
 13 rea (NRF) grant funded by the Korean government
 14 (MSIT) (No. 2021R1C1C2091550). B. L. was supported
 15 by the National Research Foundation of Korea(NRF)
 16 grant funded by the Korean government(MSIT), No.
 17 2022R1C1C1008695. D.K. acknowledges the support of
 18 the National Research Foundation of Korea (NRF) grant
 19 (No. 2021R1C1C1013580). J.H.L was supported by Basic
 20 Science Research Program through the National Re-
 21 search Foundation of Korea (NRF) funded by the Min-
 22 istry of Education (No. RS-2024-00452816).

APPENDIX

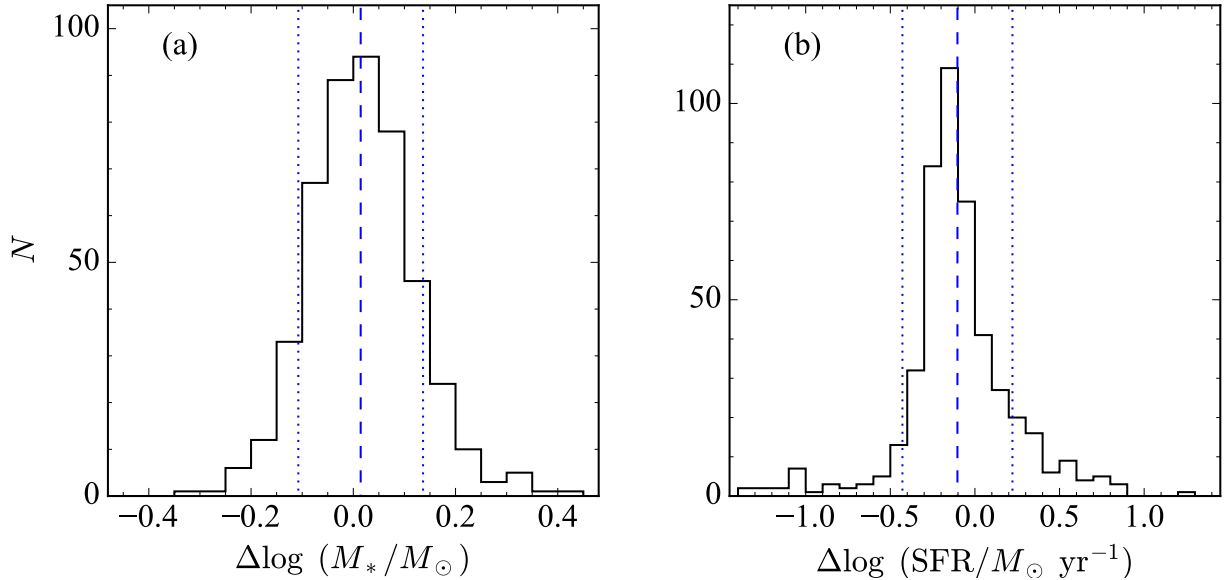


Figure A1. Histograms of differences in the stellar masses (a) and SFR (b) of the DustPedia sample between this study and Nersesian et al. (2019). The dashed and dotted lines denote the mean value and standard deviation, respectively.

A. COMPARISON WITH PREVIOUS STUDIES FOR THE DUSTPEDIA SAMPLE

For the DustPedia sample, the SED fitting with distinct fitting parameters was performed in the previous study (Nersesian et al. 2019). Specifically, the DustPedia sample was fitted with a flexible-delayed SFH, comprising both young ($t_{\text{age}} \leq 200$ Myr) and old ($t_{\text{age}} > 200$ Myr) SSPs in Nersesian et al. (2019). Among these SSPs, the old stellar population with an age range between 2 and 12 Gyr was assumed to exhibit an exponentially declining SFR, while the young stellar population was modeled with a burst or a decline of constant SFR at 200 Myr ago. The IMF of Salpeter (1955) was adopted. In addition, the dust emission was modeled using a broader range of parameters than in this study. In this appendix, we investigate systematics arising from differences in SFH and dust modeling by comparing our fitting results with those from Nersesian et al. (2019). The discrepancy in the stellar masses is nearly negligible on average [$\Delta \log (M_*/M_\odot) \equiv \log (M_*/M_\odot)(\text{this study}) - \log (M_*/M_\odot)(\text{Nersesian}) \sim 0.01$] with a scatter of ~ 0.12 dex, which may correspond to the additional uncertainty introduced by differences in SFH and IMF in the SED fitting (Fig. A1). The SFR shows a marginally larger offset and scatter [$\log (\text{SFR}/M_\odot \text{yr}^{-1}) = -0.10 \pm 0.33$ dex; Fig. A1]. However, this uncertainty will have minimal impact on this study.

B. RESIDUALS FROM THE SED FITTING IN NIR BANDS

The SED model in the NIR is highly sensitive to the choice of stellar population model, particularly based on how TP-AGB stars are treated (e.g., Maraston et al. 2006). To understand the systematics of M_*/L due to this fact, it is helpful to assess the goodness of fit by examining the NIR residuals. Figure A2 illustrates the residuals in the NIR bands (JHK_s , W1, and W2) derived from the best SED fit. Note only the results with a signal-to-noise greater than 5 are used in the experiment. Notably, the model SEDs tend to underestimate the fluxes at JHK_s , though the offsets remain within the error margin. This indicates that the NIR-based M_*/L could be marginally underestimated up to ~ 0.04 dex, although this result is not definitive.

REFERENCES

Belfiore, F., Leroy, A. K., Williams, T. G., et al. 2023, A&A, 678, A129

Bell, E. F., McIntosh, D. H., Katz, N., & Weinberg, M. D. 2003, ApJS, 149, 289

Boquien, M., Burgarella, D., Roehlly, Y., et al. 2019, A&A, 622, A103

Brown, M. J. I., Moustakas, J., Smith, J. D. T., et al. 2014, ApJS, 212, 18

Bruzual, G., & Charlot, S. 2003, MNRAS, 344, 1000

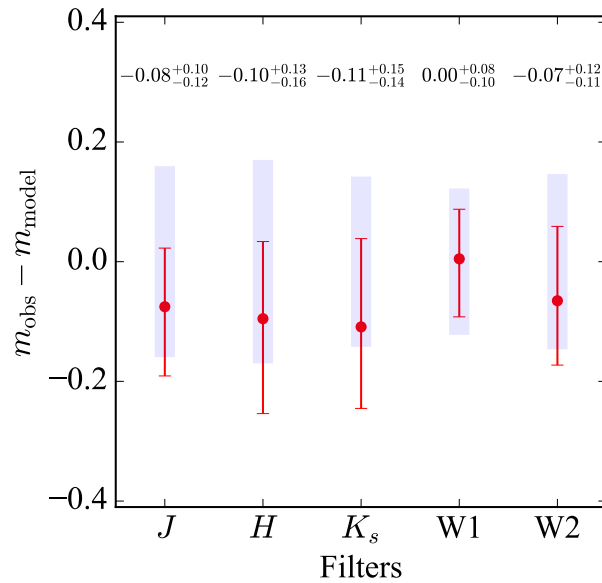


Figure A2. Distributions of residual magnitudes between the observed magnitudes (m_{obs}) and the model magnitudes (m_{model}) derived from the best-fit SED in the NIR bands (JHK_s , W1, and W2). For each filter, the median and 16/84th percentiles are displayed with the shaded region representing the typical uncertainties in the observed magnitudes.

Byun, W., Sheen, Y.-K., Seon, K.-I., et al. 2021, *ApJ*, 918, 82

Calzetti, D., Armus, L., Bohlin, R. C., et al. 2000, *ApJ*, 533, 682

Chabrier, G. 2003, *PASP*, 115, 763

Clark, C. J. R., Verstocken, S., Bianchi, S., et al. 2018, *A&A*, 609, A37

Cluver, M. E., Jarrett, T. H., Hopkins, A. M., et al. 2014, *ApJ*, 782, 90

Conroy, C. 2013, *ARA&A*, 51, 393

Conselice, C. J. 2014, *ARA&A*, 52, 291

Crill, B. P., Werner, M., Akeson, R., et al. 2020, in *Society of Photo-Optical Instrumentation Engineers (SPIE) Conference Series*, Vol. 11443, *Space Telescopes and Instrumentation 2020: Optical, Infrared, and Millimeter Wave*, ed. M. Lystrup & M. D. Perrin, 114430I

Cutri, R. M., Skrutskie, M. F., van Dyk, S., et al. 2003, *2MASS All Sky Catalog of point sources*.

Davies, J. I., Baes, M., Bianchi, S., et al. 2017, *PASP*, 129, 044102

Doré, O., Werner, M. W., Ashby, M., et al. 2016, *arXiv e-prints*, arXiv:1606.07039

Fritz, J., Franceschini, A., & Hatziminaoglou, E. 2006, *MNRAS*, 366, 767

Hon, D. S. H., Graham, A. W., Davis, B. L., & Marconi, A. 2022, *MNRAS*, 514, 3410

Inami, H., Armus, L., Matsuhara, H., et al. 2018, *A&A*, 617, A130

Inoue, A. K. 2011, *MNRAS*, 415, 2920

Into, T., & Portinari, L. 2013, *MNRAS*, 430, 2715

Jarrett, T. H., Chester, T., Cutri, R., et al. 2000, *AJ*, 119, 2498

Jarrett, T. H., Cluver, M. E., Taylor, E. N., et al. 2023, *ApJ*, 946, 95

Jones, A. P., Fanciullo, L., Köhler, M., et al. 2013, *A&A*, 558, A62

Kennicutt, R. C., & Evans, N. J. 2012, *ARA&A*, 50, 531

Kettley, T., Hesling, J., Phillipps, S., et al. 2018, *MNRAS*, 473, 776

Kim, J. H., Im, M., Lee, H. M., et al. 2012, *ApJ*, 760, 120

Kormendy, J., & Ho, L. C. 2013, *ARA&A*, 51, 511

Korngut, P. M., Bock, J. J., Akeson, R., et al. 2018, in *Society of Photo-Optical Instrumentation Engineers (SPIE) Conference Series*, Vol. 10698, *Space Telescopes and Instrumentation 2018: Optical, Infrared, and Millimeter Wave*, ed. M. Lystrup, H. A. MacEwen, G. G. Fazio, N. Batalha, N. Siegler, & E. C. Tong, 106981U

Lai, T. S. Y., Smith, J. D. T., Baba, S., Spoon, H. W. W., & Imanishi, M. 2020, *ApJ*, 905, 55

Lang, D., Hogg, D. W., & Schlegel, D. J. 2016, *AJ*, 151, 36

Larson, R. B., & Tinsley, B. M. 1978, *ApJ*, 219, 46

Lee, J. C., Hwang, H. S., Lee, M. G., Kim, M., & Lee, J. H. 2012, *ApJ*, 756, 95

Li, Y. A., Ho, L. C., Shangquan, J., Zhuang, M.-Y., & Li, R. 2023, *ApJS*, 267, 17

Lower, S., Narayanan, D., Leja, J., et al. 2020, *ApJ*, 904, 33

Madau, P., & Dickinson, M. 2014, *ARA&A*, 52, 415

Maiolino, R., & Mannucci, F. 2019, *A&A Rv*, 27, 3

Maraston, C., Daddi, E., Renzini, A., et al. 2006, *ApJ*, 652, 85

- Meidt, S. E., Schinnerer, E., Knapen, J. H., et al. 2012, *ApJ*, 744, 17
- Meidt, S. E., Schinnerer, E., van de Ven, G., et al. 2014, *ApJ*, 788, 144
- Nersesian, A., Xilouris, E. M., Bianchi, S., et al. 2019, *A&A*, 624, A80
- Norris, M. A., Van de Ven, G., Schinnerer, E., et al. 2016, *ApJ*, 832, 198
- Portinari, L., Sommer-Larsen, J., & Tantalo, R. 2004, *MNRAS*, 347, 691
- Querejeta, M., Meidt, S. E., Schinnerer, E., et al. 2015, *ApJS*, 219, 5
- Renzini, A., & Peng, Y.-j. 2015, *ApJL*, 801, L29
- Roediger, J. C., & Courteau, S. 2015, *MNRAS*, 452, 3209
- Salim, S., Boquien, M., & Lee, J. C. 2018, *ApJ*, 859, 11
- Salpeter, E. E. 1955, *ApJ*, 121, 161
- Shim, H., Hwang, H. S., Jeong, W.-S., et al. 2023, *AJ*, 165, 31
- Taylor, E. N., Hopkins, A. M., Baldry, I. K., et al. 2011, *MNRAS*, 418, 1587
- Wechsler, R. H., & Tinker, J. L. 2018, *ARA&A*, 56, 435
- Werner, M. W., Roellig, T. L., Low, F. J., et al. 2004, *ApJS*, 154, 1
- Whitcomb, C. M., Smith, J. D. T., Sandstrom, K., et al. 2024, *ApJ*, 974, 20
- Wright, E. L., Eisenhardt, P. R. M., Mainzer, A. K., et al. 2010, *AJ*, 140, 1868
- Xie, Y., Ho, L. C., Li, A., & Shangguan, J. 2018a, *ApJ*, 860, 154
- . 2018b, *ApJ*, 867, 91
- Yamada, R., Oyabu, S., Kaneda, H., et al. 2013, *PASJ*, 65, 103
- Zhang, L., & Ho, L. C. 2023, *ApJ*, 943, 60
- Zhang, L., Ho, L. C., & Xie, Y. 2021, *AJ*, 161, 29
- Zibetti, S., Charlot, S., & Rix, H.-W. 2009, *MNRAS*, 400, 1181

Table 1. Mass-to-light ratio in NIR Spectrum

λ_c	Total Luminosity						Stellar Luminosity					
	DustPedia		S82		All		DustPedia		S82		All	
	$\log(M_*/L)$	σ	$\log(M_*/L)$	σ	$\log(M_*/L)$	σ	$\log(M_*/L)$	σ	$\log(M_*/L)$	σ	$\log(M_*/L)$	σ
(1)	(2)	(3)	(4)	(5)	(6)	(7)	(8)	(9)	(10)	(11)	(12)	(13)
0.75	0.125	0.158	0.190	0.134	0.180	0.140	0.074	0.152	0.132	0.147	0.123	0.149
0.77	0.116	0.156	0.180	0.133	0.170	0.139	0.067	0.150	0.125	0.146	0.116	0.148
0.79	0.107	0.154	0.169	0.132	0.160	0.137	0.060	0.148	0.117	0.144	0.108	0.146
0.81	0.094	0.149	0.154	0.128	0.145	0.133	0.049	0.144	0.104	0.140	0.095	0.142
0.83	0.082	0.146	0.140	0.125	0.132	0.130	0.038	0.141	0.092	0.137	0.084	0.139
0.85	0.071	0.144	0.129	0.124	0.121	0.129	0.030	0.140	0.083	0.135	0.075	0.137
0.87	0.059	0.141	0.116	0.122	0.107	0.126	0.020	0.137	0.072	0.132	0.064	0.134
0.89	0.046	0.137	0.101	0.118	0.093	0.123	0.009	0.134	0.060	0.128	0.052	0.131
0.91	0.035	0.134	0.089	0.116	0.081	0.120	0.000	0.130	0.050	0.125	0.043	0.127
0.93	0.027	0.132	0.079	0.114	0.071	0.118	-0.006	0.127	0.043	0.122	0.035	0.124
0.95	0.018	0.130	0.070	0.112	0.062	0.117	-0.012	0.125	0.036	0.120	0.029	0.122
0.98	0.012	0.127	0.062	0.110	0.054	0.114	-0.018	0.124	0.029	0.118	0.022	0.120
1.00	0.005	0.124	0.054	0.108	0.047	0.112	-0.024	0.121	0.022	0.116	0.015	0.118
1.02	-0.001	0.122	0.046	0.106	0.039	0.110	-0.029	0.119	0.016	0.114	0.009	0.116
1.05	-0.008	0.121	0.039	0.106	0.032	0.110	-0.034	0.118	0.011	0.113	0.004	0.115
1.08	-0.015	0.121	0.032	0.106	0.025	0.110	-0.038	0.117	0.007	0.112	-0.000	0.114
1.10	-0.018	0.120	0.029	0.106	0.022	0.109	-0.040	0.116	0.004	0.111	-0.002	0.113
1.13	-0.020	0.118	0.026	0.104	0.019	0.108	-0.043	0.116	0.001	0.111	-0.005	0.112
1.16	-0.025	0.117	0.020	0.104	0.013	0.107	-0.047	0.115	-0.003	0.110	-0.010	0.112
1.18	-0.030	0.115	0.014	0.103	0.008	0.106	-0.051	0.114	-0.008	0.109	-0.014	0.111
1.21	-0.035	0.114	0.009	0.103	0.002	0.106	-0.055	0.113	-0.012	0.108	-0.019	0.110
1.24	-0.042	0.114	0.002	0.103	-0.005	0.106	-0.059	0.112	-0.017	0.107	-0.024	0.109
1.27	-0.050	0.114	-0.006	0.103	-0.013	0.106	-0.065	0.112	-0.023	0.107	-0.030	0.109
1.30	-0.057	0.114	-0.013	0.103	-0.020	0.106	-0.072	0.112	-0.030	0.107	-0.036	0.109
1.33	-0.063	0.113	-0.020	0.103	-0.026	0.106	-0.078	0.112	-0.036	0.107	-0.042	0.109
1.37	-0.069	0.113	-0.026	0.103	-0.033	0.106	-0.084	0.112	-0.042	0.107	-0.048	0.109
1.40	-0.076	0.112	-0.033	0.102	-0.040	0.105	-0.090	0.111	-0.048	0.106	-0.054	0.108
1.43	-0.084	0.110	-0.042	0.101	-0.049	0.104	-0.097	0.109	-0.056	0.105	-0.062	0.107
1.47	-0.096	0.108	-0.056	0.100	-0.062	0.102	-0.109	0.108	-0.068	0.103	-0.075	0.105
1.50	-0.111	0.106	-0.072	0.098	-0.078	0.101	-0.123	0.106	-0.084	0.102	-0.090	0.103
1.54	-0.127	0.105	-0.088	0.097	-0.094	0.099	-0.138	0.104	-0.100	0.100	-0.106	0.102
1.58	-0.143	0.104	-0.105	0.097	-0.110	0.099	-0.153	0.103	-0.115	0.100	-0.121	0.101
1.62	-0.157	0.103	-0.120	0.097	-0.125	0.099	-0.167	0.103	-0.130	0.099	-0.135	0.101
1.66	-0.170	0.103	-0.133	0.097	-0.139	0.099	-0.179	0.103	-0.142	0.099	-0.148	0.101
1.70	-0.180	0.104	-0.143	0.098	-0.149	0.100	-0.189	0.104	-0.152	0.100	-0.158	0.102
1.74	-0.187	0.105	-0.150	0.099	-0.156	0.101	-0.195	0.104	-0.158	0.101	-0.164	0.102
1.78	-0.191	0.105	-0.154	0.100	-0.160	0.101	-0.197	0.104	-0.161	0.101	-0.166	0.102
1.82	-0.196	0.106	-0.159	0.101	-0.165	0.102	-0.200	0.103	-0.163	0.100	-0.169	0.101
1.87	-0.203	0.108	-0.165	0.103	-0.171	0.104	-0.204	0.103	-0.168	0.100	-0.173	0.102
1.91	-0.207	0.108	-0.169	0.103	-0.175	0.105	-0.209	0.104	-0.172	0.101	-0.177	0.102
1.96	-0.209	0.107	-0.171	0.102	-0.177	0.104	-0.212	0.105	-0.174	0.102	-0.180	0.103
2.01	-0.211	0.106	-0.173	0.102	-0.179	0.103	-0.214	0.105	-0.177	0.102	-0.183	0.103
2.06	-0.215	0.106	-0.178	0.102	-0.183	0.103	-0.218	0.104	-0.181	0.101	-0.186	0.103
2.11	-0.220	0.105	-0.184	0.102	-0.189	0.103	-0.222	0.104	-0.186	0.101	-0.191	0.102
2.16	-0.225	0.105	-0.189	0.102	-0.195	0.103	-0.226	0.103	-0.190	0.100	-0.196	0.101
2.21	-0.226	0.104	-0.191	0.102	-0.196	0.103	-0.226	0.102	-0.191	0.100	-0.197	0.101
2.26	-0.221	0.105	-0.186	0.102	-0.191	0.104	-0.222	0.103	-0.186	0.100	-0.192	0.101

Table 1 *continued*

Table 1 (continued)

λ_c	Total Luminosity						Stellar Luminosity					
	DustPedia		S82		All		DustPedia		S82		All	
	$\log (M_*/L)$	σ	$\log (M_*/L)$	σ	$\log (M_*/L)$	σ	$\log (M_*/L)$	σ	$\log (M_*/L)$	σ	$\log (M_*/L)$	σ
(1)	(2)	(3)	(4)	(5)	(6)	(7)	(8)	(9)	(10)	(11)	(12)	(13)
2.32	-0.211	0.108	-0.174	0.105	-0.180	0.106	-0.211	0.105	-0.173	0.102	-0.179	0.104
2.38	-0.198	0.109	-0.160	0.106	-0.166	0.108	-0.197	0.107	-0.159	0.103	-0.164	0.105
2.43	-0.187	0.109	-0.148	0.106	-0.154	0.107	-0.185	0.106	-0.146	0.102	-0.152	0.103
2.49	-0.180	0.108	-0.141	0.105	-0.147	0.107	-0.177	0.105	-0.138	0.100	-0.144	0.102
2.55	-0.187	0.109	-0.148	0.107	-0.154	0.108	-0.183	0.105	-0.143	0.101	-0.150	0.103
2.61	-0.207	0.112	-0.166	0.110	-0.173	0.111	-0.201	0.107	-0.161	0.103	-0.167	0.104
2.68	-0.224	0.114	-0.183	0.112	-0.189	0.113	-0.218	0.109	-0.177	0.105	-0.183	0.107
2.74	-0.237	0.116	-0.195	0.114	-0.202	0.115	-0.231	0.112	-0.189	0.107	-0.195	0.109
2.81	-0.245	0.116	-0.204	0.115	-0.210	0.116	-0.239	0.112	-0.196	0.107	-0.203	0.109
2.88	-0.247	0.114	-0.207	0.113	-0.213	0.114	-0.239	0.109	-0.199	0.105	-0.205	0.106
2.95	-0.244	0.110	-0.208	0.110	-0.213	0.111	-0.236	0.104	-0.197	0.100	-0.203	0.101
3.02	-0.245	0.107	-0.210	0.109	-0.215	0.109	-0.233	0.099	-0.197	0.096	-0.203	0.098
3.09	-0.254	0.110	-0.221	0.115	-0.226	0.115	-0.235	0.097	-0.201	0.095	-0.206	0.096
3.17	-0.286	0.129	-0.255	0.142	-0.260	0.141	-0.239	0.097	-0.206	0.095	-0.211	0.096
3.25	-0.341	0.163	-0.310	0.186	-0.315	0.183	-0.246	0.099	-0.213	0.097	-0.218	0.098
3.32	-0.365	0.175	-0.333	0.201	-0.338	0.197	-0.256	0.102	-0.221	0.100	-0.226	0.101
3.40	-0.341	0.155	-0.308	0.175	-0.313	0.172	-0.266	0.106	-0.230	0.104	-0.235	0.105
3.49	-0.310	0.132	-0.276	0.143	-0.281	0.142	-0.273	0.109	-0.236	0.107	-0.241	0.108
3.57	-0.298	0.124	-0.264	0.131	-0.269	0.130	-0.275	0.109	-0.238	0.107	-0.244	0.108
3.66	-0.294	0.121	-0.261	0.128	-0.266	0.127	-0.273	0.107	-0.237	0.105	-0.243	0.106
3.75	-0.291	0.119	-0.260	0.127	-0.265	0.126	-0.269	0.104	-0.235	0.103	-0.240	0.104
3.84	-0.291	0.119	-0.261	0.128	-0.265	0.127	-0.266	0.102	-0.233	0.101	-0.238	0.102
3.93	-0.297	0.123	-0.267	0.133	-0.271	0.132	-0.268	0.103	-0.235	0.102	-0.240	0.103
4.03	-0.308	0.129	-0.276	0.140	-0.281	0.139	-0.274	0.106	-0.239	0.104	-0.244	0.105
4.13	-0.316	0.132	-0.283	0.144	-0.288	0.143	-0.280	0.108	-0.244	0.107	-0.250	0.108
4.23	-0.318	0.134	-0.285	0.147	-0.290	0.146	-0.283	0.111	-0.246	0.109	-0.252	0.110
4.33	-0.316	0.136	-0.284	0.151	-0.289	0.150	-0.279	0.112	-0.241	0.110	-0.247	0.111
4.43	-0.313	0.139	-0.283	0.157	-0.287	0.154	-0.271	0.111	-0.234	0.110	-0.240	0.111
4.54	-0.312	0.142	-0.284	0.162	-0.288	0.159	-0.265	0.110	-0.229	0.108	-0.234	0.109
4.65	-0.316	0.145	-0.289	0.166	-0.293	0.164	-0.263	0.108	-0.228	0.107	-0.233	0.108
4.77	-0.323	0.148	-0.297	0.172	-0.301	0.169	-0.264	0.107	-0.229	0.106	-0.235	0.107
4.88	-0.333	0.154	-0.307	0.179	-0.311	0.176	-0.265	0.107	-0.231	0.106	-0.236	0.107
5.00	-0.347	0.162	-0.323	0.190	-0.326	0.187	-0.267	0.106	-0.233	0.106	-0.238	0.106

NOTE— Col. (1): Central wavelength of the luminosity in units of μm . Col. (2): logarithmic M_*/L of the DustPedia sample based on the total luminosity. Col. (3): Scatter (dex) in M_*/L of the DustPedia sample based on the total luminosity. Col. (4): logarithmic M_*/L of the S82 sample based on the total luminosity. Col. (5): Scatter (dex) in logarithmic M_*/L of the S82 sample based on the total luminosity. Col. (6): logarithmic M_*/L of the entire sample based on the total luminosity. Col. (7): Scatter (dex) in logarithmic M_*/L of the entire sample based on the total luminosity. Col. (8): M_*/L of the DustPedia sample based on the stellar luminosity. Col. (9): Scatter (dex) in logarithmic M_*/L of the DustPedia sample based on the stellar luminosity. Col. (10): M_*/L of the S82 sample based on the stellar luminosity. Col. (11): Scatter (dex) in logarithmic M_*/L of the S82 sample based on the stellar luminosity. Col. (12): M_*/L of the entire sample based on the stellar luminosity. Col. (13): Scatter (dex) in logarithmic M_*/L of the entire sample based on the stellar luminosity.

Table 2. $\log (M_*/L) = a + b \log (M_*/M_\odot)$

λ_c	a	b	σ
(1)	(2)	(3)	(4)
0.75	-1.344	0.141	0.130
0.77	-1.338	0.139	0.129
0.79	-1.327	0.138	0.127
0.81	-1.297	0.134	0.123
0.83	-1.277	0.130	0.121
0.85	-1.270	0.129	0.119
0.87	-1.251	0.126	0.117
0.89	-1.219	0.122	0.114
0.91	-1.184	0.118	0.111
0.93	-1.156	0.114	0.109
0.95	-1.136	0.112	0.107
0.98	-1.116	0.109	0.106
1.00	-1.090	0.106	0.104
1.02	-1.065	0.103	0.103
1.05	-1.052	0.101	0.102
1.08	-1.046	0.100	0.101
1.10	-1.040	0.099	0.100
1.13	-1.036	0.099	0.100
1.16	-1.030	0.098	0.100
1.18	-1.021	0.096	0.099
1.21	-1.010	0.095	0.098
1.24	-1.003	0.094	0.098
1.27	-1.001	0.093	0.097
1.30	-1.005	0.093	0.097
1.33	-1.012	0.093	0.097
1.37	-1.019	0.093	0.097
1.40	-1.024	0.093	0.096
1.43	-1.019	0.092	0.095
1.47	-1.008	0.089	0.094
1.50	-0.993	0.087	0.093
1.54	-0.982	0.084	0.092
1.58	-0.979	0.082	0.091
1.62	-0.974	0.080	0.091
1.66	-0.966	0.078	0.092
1.70	-0.965	0.077	0.093
1.74	-0.971	0.077	0.094
1.78	-0.973	0.077	0.094
1.82	-0.974	0.077	0.093
1.87	-0.984	0.078	0.093
1.91	-0.997	0.079	0.094
1.96	-1.005	0.079	0.094
2.01	-1.004	0.079	0.094
2.06	-0.993	0.077	0.094
2.11	-0.979	0.076	0.094
2.16	-0.961	0.073	0.094
2.21	-0.947	0.072	0.093
2.26	-0.958	0.073	0.094
2.32	-0.993	0.078	0.095
2.38	-1.023	0.082	0.095

Table 2 *continued*

Table 2 (*continued*)

λ_c	a	b	σ
(1)	(2)	(3)	(4)
2.43	-1.034	0.085	0.093
2.49	-1.050	0.087	0.091
2.55	-1.076	0.089	0.092
2.61	-1.106	0.090	0.093
2.68	-1.138	0.092	0.095
2.74	-1.163	0.093	0.097
2.81	-1.165	0.092	0.098
2.88	-1.131	0.089	0.096
2.95	-1.071	0.083	0.092
3.02	-1.013	0.078	0.089
3.09	-0.977	0.074	0.088
3.17	-0.958	0.072	0.089
3.25	-0.955	0.071	0.091
3.32	-0.975	0.072	0.094
3.40	-1.007	0.074	0.098
3.49	-1.025	0.075	0.100
3.57	-1.019	0.074	0.101
3.66	-0.992	0.072	0.099
3.75	-0.955	0.069	0.097
3.84	-0.932	0.067	0.096
3.93	-0.938	0.067	0.097
4.03	-0.966	0.069	0.099
4.13	-0.999	0.072	0.101
4.23	-1.020	0.074	0.103
4.33	-1.019	0.074	0.104
4.43	-0.999	0.073	0.104
4.54	-0.972	0.071	0.103
4.65	-0.951	0.069	0.102
4.77	-0.942	0.068	0.101
4.88	-0.935	0.067	0.101
5.00	-0.929	0.066	0.101

NOTE— Col. (1): Central wavelength of the luminosity in units of μm . Col. (2): Intercept in the linear regression fit between logarithmic stellar mass in units of the solar mass and logarithmic M_*/L . Col. (3): Slope in the linear regression fit between logarithmic stellar mass in units of the solar mass and logarithmic M_*/L . Col. (4): Scatter (dex) in logarithmic M_*/L .

Table 3. $\log (M_*/L) = a \left\{ \frac{1}{2} \left[1 + \left(\frac{\log \text{sSFR}}{\delta} \right)^{1/\beta} \right] \right\}^{-\alpha\beta}$

λ_c	a	δ	β	α	σ
(1)	(2)	(3)	(4)	(5)	(6)
0.75	0.180	0.0114	1.041	0.320	0.057
0.77	0.172	0.0113	1.053	0.315	0.058
0.79	0.163	0.0113	1.064	0.309	0.059
0.81	0.151	0.0109	1.046	0.298	0.056
0.83	0.141	0.0106	1.031	0.290	0.054
0.85	0.132	0.0104	1.027	0.285	0.053
0.87	0.123	0.0101	0.999	0.279	0.049
0.89	0.114	0.0097	0.953	0.270	0.044
0.91	0.106	0.0093	0.911	0.262	0.038
0.93	0.101	0.0090	0.879	0.255	0.035
0.95	0.095	0.0087	0.852	0.249	0.032
0.98	0.090	0.0084	0.824	0.244	0.029
1.00	0.085	0.0082	0.795	0.238	0.027
1.02	0.080	0.0080	0.768	0.233	0.025
1.05	0.075	0.0079	0.752	0.229	0.024
1.08	0.071	0.0077	0.746	0.226	0.024
1.10	0.069	0.0076	0.742	0.223	0.023
1.13	0.066	0.0075	0.736	0.221	0.023
1.16	0.062	0.0074	0.726	0.219	0.023
1.18	0.058	0.0073	0.717	0.217	0.022
1.21	0.054	0.0072	0.708	0.214	0.022
1.24	0.049	0.0071	0.698	0.211	0.022
1.27	0.044	0.0070	0.689	0.209	0.022
1.30	0.038	0.0070	0.682	0.208	0.022
1.33	0.032	0.0069	0.681	0.208	0.022
1.37	0.026	0.0068	0.684	0.207	0.022
1.40	0.020	0.0068	0.691	0.205	0.022
1.43	0.010	0.0067	0.692	0.202	0.022
1.47	-0.002	0.0066	0.680	0.198	0.022
1.50	-0.017	0.0065	0.658	0.193	0.022
1.54	-0.033	0.0064	0.639	0.189	0.022
1.58	-0.049	0.0064	0.624	0.186	0.023
1.62	-0.062	0.0063	0.605	0.184	0.024
1.66	-0.074	0.0063	0.582	0.183	0.027
1.70	-0.083	0.0063	0.564	0.183	0.029
1.74	-0.089	0.0063	0.559	0.184	0.030
1.78	-0.092	0.0062	0.565	0.183	0.030
1.82	-0.095	0.0062	0.574	0.182	0.029
1.87	-0.099	0.0062	0.578	0.183	0.028
1.91	-0.103	0.0062	0.577	0.184	0.029
1.96	-0.105	0.0062	0.577	0.185	0.029
2.01	-0.107	0.0062	0.573	0.185	0.029
2.06	-0.111	0.0062	0.563	0.183	0.030
2.11	-0.117	0.0062	0.550	0.181	0.032
2.16	-0.122	0.0062	0.538	0.179	0.034
2.21	-0.123	0.0062	0.532	0.177	0.034
2.26	-0.117	0.0062	0.537	0.179	0.034
2.32	-0.103	0.0062	0.555	0.185	0.031
2.38	-0.088	0.0062	0.581	0.189	0.028

Table 3 continued

Table 3 (*continued*)

λ_c	a	δ	β	α	σ
(1)	(2)	(3)	(4)	(5)	(6)
2.43	-0.077	0.0063	0.621	0.189	0.024
2.49	-0.072	0.0063	0.677	0.189	0.022
2.55	-0.079	0.0064	0.710	0.190	0.022
2.61	-0.094	0.0063	0.703	0.193	0.023
2.68	-0.108	0.0062	0.685	0.196	0.023
2.74	-0.118	0.0062	0.672	0.200	0.024
2.81	-0.125	0.0062	0.663	0.200	0.024
2.88	-0.129	0.0062	0.657	0.194	0.024
2.95	-0.131	0.0061	0.651	0.185	0.023
3.02	-0.133	0.0061	0.636	0.177	0.024
3.09	-0.136	0.0061	0.610	0.172	0.026
3.17	-0.141	0.0060	0.581	0.170	0.029
3.25	-0.146	0.0060	0.555	0.171	0.032
3.32	-0.152	0.0061	0.535	0.176	0.035
3.40	-0.063	0.0155	0.007	0.259	0.044
3.49	-0.062	0.0153	0.007	0.259	0.046
3.57	-0.062	0.0153	0.007	0.258	0.047
3.66	-0.062	0.0155	0.007	0.258	0.047
3.75	-0.062	0.0158	0.007	0.257	0.048
3.84	-0.062	0.0159	0.007	0.255	0.048
3.93	-0.062	0.0159	0.007	0.256	0.048
4.03	-0.062	0.0157	0.007	0.256	0.049
4.13	-0.062	0.0155	0.007	0.257	0.049
4.23	-0.062	0.0152	0.007	0.257	0.050
4.33	-0.062	0.0151	0.007	0.258	0.051
4.43	-0.159	0.0060	0.487	0.185	0.047
4.54	-0.155	0.0060	0.482	0.182	0.048
4.65	-0.155	0.0060	0.477	0.179	0.048
4.77	-0.157	0.0060	0.474	0.177	0.048
4.88	-0.062	0.0156	0.007	0.257	0.053
5.00	-0.062	0.0157	0.007	0.257	0.053

NOTE— Col. (1): Central wavelength of the luminosity in units of μm . Col. (2): Normalization factor in the smoothly broken power law fit, which is equivalent to $\log(M_*/L)$ at $\text{sSFR} \ll \delta$. Note that the unit of sSFR is Gyr^{-1} . Col. (3): Pivot sSFR in units of Gyr^{-1} . Col. (4): Smoothness parameter. Col. (5): Power-law index above the pivot sSFR . Col. (6): Scatter (dex) in logarithmic M_*/L .